Enhancement of direct electron transfer in graphene bioelectrodes containing novel cytochrome c_{553} variants with optimized heme orientation

Miriam Izzo [a], Silvio Osella [b,*], Margot Jacquet [a], Małgorzata Kiliszek [a], Ersan Harputlu [c], Alicja Starkowska [b], Anna Łasica [d], C. Gokhan Unlu [e], Tomasz Uśpieński [f], Paweł Niewiadomski [f], Dariusz Bartosik [d], Bartosz Trzaskowski [b], Kasim Ocakoglu [c], Joanna Kargul [a,*]

[a] Solar Fuels Laboratory, Center of New Technologies, University of Warsaw, Banacha 2C, 02-097 Warsaw, Poland
[b] Chemical and Biological Systems Simulation Lab, Center of New Technologies, University of Warsaw, Banacha 2C, 02-097 Warsaw, Poland
[c] Department of Engineering Fundamental Sciences, Faculty of Engineering, Tarsus University, 33400 Tarsus, Turkey
[d] Department of Bacterial Genetics, Institute of Microbiology, Faculty of Biology, University of Warsaw, Miecznikowa 1, 02-096 Warsaw, Poland
[e] Department of Biomedical Engineering, Pamukkale University, TR-20070 Denizli, Turkey
[f] Laboratory of Molecular and Cellular Signaling, Center of New Technologies, University of Warsaw, Banacha 2C, 02-097 Warsaw, Poland

ARTICLE INFO

ABSTRACT

The highly efficient bioelectrodes based on single layer graphene (SLG) functionalized with pyrene self-assembled monolayer and novel cytochrome c_{553} (cyt c_{553}) peptide linker variants were rationally designed to optimize the direct electron transfer (DET) between SLG and the heme group of cyt. Through a combination of photoelectrochemical and quantum mechanical (QM/MM) approaches we show that the specific amino acid sequence of a short peptide genetically inserted between the cyt c_{553}-holoprotein and the surface anchoring C-terminal His$_6$-tag plays a crucial role in ensuring the optimal orientation and distance of the heme group with respect to the SLG surface. Consequently, efficient DET occurring between graphene and cyt c_{553} leads to a 20-fold enhancement of the cathodic photocurrent output compared to the previously reported devices of a similar type. The QM/MM modeling implies that a perpendicular or parallel orientation of the heme group with respect to the SLG surface is detrimental to DET, whereas the tilted orientation favors the cathodic photocurrent generation. Our work confirms the possibility of fine-tuning the electronic communication within complex bio-organic nanoarchitectures and interfaces due to optimization of the tilt angle of the heme group, its distance from the SLG surface and optimal HOMO/LUMO levels of the interacting redox centers.

1. Introduction

The successful generation of hybrid materials that incorporate artificial and natural molecular components into a working system for light-harvesting and energy conversion has been recently advanced by combining various synthetic and biological photo-electroactive components including photosystems and other light harvesting proteins, semiconductors as well as graphene and its derivatives [1–5]. The current challenge remains to apply a rational design of such biomolecular assemblies so as to ensure the optimal direct electron transfer (DET) upon light activation in which the wasteful back reactions are minimized [6–8].

One of the key factors for improving the power conversion efficiency of solar-to-fuel devices or to enhance the sensitivity for biosensors is to engineer efficient DET at the interface between the electrode surface and the (photo)electroactive molecules. To this end, the rational design used in the previous studies aimed to achieve a specific orientation of the electroactive biological components with respect to the electrode surface [9,10], ensure the optimal distance between the redox-active groups of the biocomponents and the electrode surface [11,12], expose the redox-active sites to enhance the DET kinetics inside the nanode-vices, or use the molecular wiring approach for immobilization of tightly coupled electroactive proteins on the electrode surface [13].

One of the most widely investigated redox-active protein in bio-electrochemistry is cytochrome *c* (cyt *c*) [14]. The biomolecule has been used as a model biotic component to dissect the intricate DET processes occurring between the redox-active heme group of cyt *c* and the electrode surface [15–18]. To this end, various types of organic conductive interfaces and electrode materials were used including gold [16,19], semiconductors [19,15], conductive materials [20] and graphene [21,22].

The cyt c_6 protein (and its close homologue cyt c_{553} from extremophilic red microalgae, used in the present study) is involved in the primary events of energy conversion in natural photosynthesis, i.e. reduction of photo-oxidized $P700^+$ reaction center of photosystem I (PSI), a key solar-converting macromolecular machine operating in the fundamental process of oxygenic photosynthesis. The electroactive cyt *c* protein, physically and electronically interacting with PSI during solar-driven photosynthetic electron transfer (ET), has been successfully used as the biological conductive interface (biological wire) in the hybrid solar cells and solar-to-fuel devices. It was also used as the PSI-orienting molecule for enhancement of photocurrent output and improvement of optical properties of the PSI photoactive module [15,19,21–24]. In addition, a strong evidence of cyt *c* importance as the essential ET cofactor shuttling between an arbitrary sacrificial electron source and PSI was provided by the observation that in the absence of this protein there was no *in vitro* H_2 production in solar-to-fuel systems [25].

Of various materials applied for construction of biomolecular photoelectrochemical devices, graphene provides an excellent choice due to its semi-metal nature, two-dimensional structure susceptible to various types of functionalization and unique electronic properties. Graphene and its derivatives has been shown to be an efficient acceptor of energy in various architectures, including graphene/semiconductor [26], graphene/polymer [27], and graphene/light-harvesting complex [28]. The linear dispersion of the valence and conduction bands at the high K symmetry point and the point degeneration of the two bands, make graphene an ambipolar material, able to efficiently transfer either electrons or vacancies with measured mobilities for a suspended monolayer exceeding 50,000 $cm^2V^{-1}s^{-1}$ in ambient conditions [29]. The tunability of charge carriers and the impressive electron mobility make graphene the material of choice to enhance the DET in biohybrid electronic devices. Yet, the peculiar electronic properties of graphene also mean that it is a zero-bandgap material, and to obtain a well-working device a bandgap, even a small one, is needed. One successful strategy to overcome the zero-bandgap problem is to build an interface in which the conductive bioorganic self-assembled monolayer (SAM) is physisorbed onto graphene, allowing for the opening of a gap in this material and an increase of DET either to or from graphene. Such a strategy provides fine tuning of the energy levels of the frontier orbitals since the SAM-graphene interaction governs the charge flow direction. The physisorption of SAM onto the graphene surface allows the preservation of the high conductive properties of the latter material, i.e. high mobility of free electrons, to form non-covalent functional structures with molecules containing common π-systems, such as pyrene and its derivatives. This strategy results in generation of a molecular conductive interface between the electroactive biotic component (e.g. cyt *c*) and the graphene monolayer [15,22].

In this work, we constructed a novel class of biophotoelectrodes based on single layer graphene (SLG) and cyt c_{553} peptide linker variants differing in the orientation and distance of the heme group with respect to the SLG surface. This nanosystem allowed us to probe electrochemically and theoretically the intricate properties of DET between the heme group, organic interface and graphene monolayer. Our study shows that the amino acid sequence of the peptide linkers, genetically inserted between the cyt c_{553} holoprotein and the *C*-terminal His$_6$-tag anchor, plays a crucial role in

ensuring the optimal orientation and distance of the heme redox group with respect to the SLG surface for the efficient DET between the biotic and abiotic components. Theoretical mechanistic model of DET shows that a tilted orientation of heme promotes the cathodic photocurrent generation as observed for the specific novel class of the cyt-based hybrid nanodevices reported in this study.

2. Materials and methods

2.1. Design of peptide linkers

The novel peptide linkers were designed and selected according with the lowest level of calculated 2D Gibbs free energy maps using PyRosetta® software [30], according to the previous study [15]. These maps included relative counts of energetically permissive conformations for a given orientation of a heme plane described by its distance to the electrode plane and the angle between the two planes. The maps also showed the number of conformations in a logarithmic scale, a parameter that is right proportional to the Gibbs free energy of a given state. The 7 AA sequences, generated randomly, displayed the minimal levels of Gibbs free energy (between 70 and 120 R.U.). As a control, a 19AA peptide linker was used which was previously applied for the optimization of performance of PSI-based photoelectrodes (see Table 1 for AA sequences) [22].

2.2. Genetic engineering of the cytochrome c_{553} variants

Recombinant DNA techniques were performed according to [31]. The *petJ* gene, annotated CMV209C in *Cyanidioschyzon merolae* genome database [32], encoding for the cyt c_{553} protein was cloned *de novo* in *Escherichia coli* in three different variants, so that the final expressed proteins consisted of the unique 7AA peptide linkers (L1-L3) inserted between the cyt c_{553} holoprotein and its *C*-terminal His$_6$-tag. The cDNA inserts encoding three genetically engineered cyt c_{553} variants (synthesized *de novo* by GeneArt®) were excised from the pMA cloning vector with PstI and NcoI restriction enzymes. The correct size of the inserts (430 bp) was confirmed by agarose DNA electrophoresis, as shown in Fig. S1A. The digested products were purified by using a GeneJET Gel Extraction Kit (Thermo Scientific™). Subsequently, the inserts were ligated with the pBAD/HisA expression vector and the resulting recombinant plasmids were transformed into *E. coli* Top10 chemicompetent cells. The *E. coli* cells harboring the novel constructs (pBAD/HisA/petJ/L1/His$_6$; pBAD/HisA/petJ/L2/His$_6$; pBAD/HisA/petJ/L3/His$_6$) were additionally co-transformed with a pEC86 plasmid encoding the heme maturation cassette. The expression of the recombinant cyt c_{553} variants in *E. coli* was conducted as described previously [15]. DNA restriction analysis of all the recombinant plasmids confirmed the successful ligation of the L1-L3 fragments to the pBAD/HisA/petJ expression constructs, as shown in Fig. S1B.

Table 1
Amino acid sequences of the novel His$_6$-tagged cyt c_{553} variants.

Name of cyt c_{553} variant	AA sequence of linker peptides	Linker length (AA number)	Molecular weight of cyt c_{553} variant (kDa)
7 AA (L1)	Cyt-QGTRGRT-HHHHHH	7	12.91
7 AA (L2)	Cyt-FSILVMS-HHHHHH	7	12.93
7 AA (L3)	Cyt-CICQRMH-HHHHHH	7	13.03
19 AA[*]	Cyt-AEAAAKEAAAKEAAA KALE-HHHHHH	19	13.95

[*] 19AA cyt c_{553} control variant obtained in the study of Janna Olmos et al. (2017) [15].

2.3. Expression and purification of the novel peptide linker cytochrome c_{553} variants

The purification of the three novel peptide linker variants of His$_6$-tagged cyt c_{553} (dubbed L1-L3) was conducted by HPLC using an Immobilized Metal Affinity Chromatography (IMAC) approach with a preparative Ni-NTA HisTrap™ column (GE Healthcare). Filtered *E. coli* cell extracts obtained by sonication were applied onto a HisTrap™ column at a flow rate of 0.5 mL/min. The specifically bound proteins were washed for 40 min. at a flow rate of 0.5 mL/min. with 20 mM imidazole and then eluted using a linear 50 mM – 500 mM imidazole gradient. The L1-L3 cyt c_{553} variants were eluted after a 10 min. wash with 500 mM imidazole. The elution was conducted at a flow rate of 1 mL/min. The purification procedure was monitored at the cyt c_{553}-specific wavelength of 553 nm. The purified cyt c_{553} variants were concentrated using the VIVASPIN-2 devices with 3,000 MWCO (WITKO, Poland) and resuspended in a 5 mM phosphate buffer (pH 7) supplemented with 25% glycerol (w/v). The concentration of the redox-active cyt c_{553} protein was determined at room temperature (RT) using absorption difference spectroscopy, as described in [15]. Briefly, the amplitude of the redox difference peak at 553 nm for oxidized – reduced cyt c_{553} spectra was used to calculate the concentration of each variant using the extinction coefficient of 24.1 mM^{-1} cm^{-1}.

2.4. Preparation of single layer graphene and its transfer onto FTO

The procedure for the generation of single layer graphene (SLG) was performed as described in [22]. Briefly, SLG was produced using a Cu foil as a catalyst *via* a chemical vapor deposition (CVD) method, then transferred onto an FTO substrate (1.5 cm × 1.5 cm). The obtained SLG on FTO was analyzed using Raman scattering spectroscopy. The intactness of the SLG monolayer on the FTO surface was confirmed with field emission-scanning electron microscopy (FE-SEM), polarized light microscopy, and atomic force microscopy.

2.5. Biofunctionalization of SLG

The bioelectrodes based on SLG were functionalized with pyrene-nitrilotriacetic acid (pyr-NTA-Ni^{2+}) SAM followed by incubation with each His$_6$-tagged cyt c_{553} variant. Briefly, FTO/SLG electrodes were sonicated in acetone for 1 min., then dried for 10 min. at RT. Subsequently, they were incubated with 30 μL of 2 mM of pyrene-NTA (pyr-NTA) for 1 h. Dried electrodes were incubated for 1 h with 100 mM NiSO$_4$ followed by a 2-h incubation with each cyt c_{553} peptide linker variant (30 μM) in 5 mM phosphate buffer at RT. The unbound cyt was removed by gentle rinsing of the electrode surface with 5 mM phosphate buffer.

2.6. Scanning electron microscopy analysis

Electron microscope images were recorded using an ultrahigh-resolution SU8200 Hitachi FE-SEM. Samples were engraved with a regular head diamond tip glass cutter. The selected fragments of the devices were coated with gold before visualization.

2.7. Electrochemical analysis

The electrochemical measurements were performed with the AUTOLAB potentiostat/galvanostat (Metrohm Autolab B.V., the Netherlands) connected with a halogen white light source (Schott, KL 2500 LCD, Germany) for conducting photoelectrochemical measurements. All experiments were carried out in a Teflon-made three-electrode cell filled with 5 mM phosphate buffer (pH 7.0) as an electrolyte. The FTO glass (1.5 cm × 1.5 cm) modified with SLG/pyr-NTA-Ni/cyt nanoconstruct served as a working electrode (WE) connected through the copper tape with a conductive adhesive (6.4 mm width) in order to provide electrical contact. The geometric active surface area of the WE was calculated as 0.4185 cm^2 based on Viton O-rings with the internal diameter of 7.30 mm used as a contact with the electrolyte. The Ag/AgCl electrode was used as a reference electrode (RE), whilst a glassy carbon rod served as a counter electrode (CE). The photochronoamperometric measurements were performed under aerobic conditions at various potentials in the dark and in the presence of the light of 100 mW·cm^{-2} intensity (1 sun) with a 'light ON/OFF' period of 30 s. Before each experiment, open circuit potential (OCP) was recorded in order to achieve a stable potential value. Cyclic voltammetry (CV) analysis was carried out in the dark in an Ar-saturated electrolyte. Freshly functionalized electrodes were subjected to voltammetric potential cycling at the scan rate of 5 mV·s^{-1} in the potential range from 0.5 V to −0.05 V. In order to assure reproducibility of the electrode preparation and its performance, (photo)electrochemical experiments were conducted at least twice. All the electrochemical data were obtained in the absence of any exogenous artificial mediators.

2.8. Theoretical simulations

Considering the complexity of the studied systems, a multiscale computational approach was used in order to describe the conformational orientations and the electronic properties of the interfaces. With the use of force-field-based methods the time-evolution of full-atom models was computed for the three different interfaces in which the peptide linker cyt variants were used as described in Table 1. Classical Molecular Dynamic (MD) simulations were carried out using a GROMACS 2018 program [33,34] and CHARM36 force-field, with the time-step of 2 fs and total simulation time of 200 ns at 300 K, in the NVT ensemble (see Supporting Information for more details). For each interface with different linker (L1, L2 and L3), two independent MD simulations were performed to enhance the statistical significance of the analysis. The results reported here refer to the average of the two simulations for each interface. From the equilibrated MD trajectories, 50 snapshots were extracted in the last 20 ns of the MD trajectory and used as input structures for Quantum Mechanics / Molecular Mechanics (QM/MM) calculations. Within the QM/MM method, the heme/NTA pair was described at the Density-functional theory (DFT) level while the environment (cytochrome) was described using the electrostatic embedding scheme, which allows the description of the environment without neglecting inhomogeneity. Since the final device is of an all-solid-state type, solvent molecules and ions were not considered. The CAM-B3LYP functional [35] together with the frozen-core LACV3P** basis set [36] were used throughout the whole study, as implemented within the Jaguar v.8.0 program [37]. For each structure pair extracted, a single point calculation was performed, and electronic properties were analyzed. The details of the methodology, which was also used in our previous study [38], are described in the Supporting Information.

3. Results and discussion

3.1. Rational design, genetic engineering and biochemical characterization of the novel cytochrome c_{553} variants

In this study, we constructed a novel class of biophotoelectrodes based on SLG and 7AA peptide linker variants of cyt c_{553} differing in the orientation and distance of the heme group with respect to the SLG surface. The model electroactive protein used

here is the robust cyt c_{553} from an extremophilic red microalga *Cyanidioschyzon merolae*. It is a Class I *c*-type cyt in which the redox-active heme group is covalently bound to Cys34 and Cys37 residues and the central Fe atom displays octahedral coordination with His18 and Met58 axial ligands [39].

The three novel peptide linker variants (designated L1-L3) were designed based on our earlier *in silico* study, in which we identified several 7AA peptides characterized by the lowest free Gibbs energy, and which were all predicted to exhibit a small degree of rotational movement of cyt c_{553} molecule upon its immobilization on the electrode surface, providing the means for the optimal orientation and distance of the heme group with respect to the electrode surface (see Table 1) [15].

In the previous study, we generated a library of cyt c_{553} variants, containing peptide linkers of varying length between the cyt holoprotein and a *C*-terminal His$_6$-tag used to anchor this protein onto the electrode surface [15]. The library comprised cyt c_{553} variants with 0, 5, 10, 12 and 19 AA linkers. The *in silico* generated 7AA linker population provided a new class of peptide linkers that were omitted in the experimental design of the previous study [15]. Importantly, theoretical simulations revealed the existence of the specific peptide sequences within the 7AA linker population that exhibited more suitable, i.e. minimal levels of the Gibbs free energy in conjunction with the reasonable rotational flexibility compared to the experimental linkers of the same study. We postulated that these characteristics together with the theoretically predicted increased conformational flexibility of the subpopulation of 7AA linkers compared to the shorter peptides [15] could be beneficial for the kinetics of DET between the SLG electrode and heme. Our present study aimed to verify this hypothesis. Another reason behind the specific 7AA peptide sequence choice was to obtain a more heterogeneous amino acid chains to probe the effects of the actual amino acid sequence within the same peptide length on the DET properties.

The selected L1-L3 peptide linkers were genetically engineered between the *C*-terminus of cyt c_{553} holoprotein and the His$_6$-tag, the latter used to strongly capture this protein on the appropriately functionalized SLG surface. We cloned and overexpressed the transgenes encoding all the three 7AA peptide linker variants of cyt c_{553} in *E. coli* using the tightly catabolically controlled co-expression system combined with the constitutive expression of the heme maturation cassette. The L1-L3 His$_6$-tagged cyt c_{553} variants were purified to homogeneity using an IMAC approach (Fig. 1A). Western blot analysis confirmed the presence of a His$_6$-tag in all the 7AA cyt c_{553} variants used in this study (Fig. 1B). We confirmed the redox activity of the purified L1-L3 cyt c_{553} variants using redox difference absorption spectroscopy

by observing the disappearance of 553-nm and 521-nm heme-derived peaks upon full chemical oxidation (see Fig. S2). The total yield of redox-active cyt c_{553} variants was estimated in the range of 7–15 mg·L^{-1}.

3.2. Construction and electrochemical characterization of the novel cytochrome-functionalized graphene photoelectrodes

Three distinct bioelectrodes were constructed by functionalization of the SLG/FTO/glass substrate with the His$_6$-tagged 7AA cyt c_{553} variants (designated L1-L3). As a conductive interface between the biotic and abiotic modules we used a pyrene derivative (pyr-NTA) SAM coordinated with a Ni^{2+} cation for capturing the *C*-terminal His$_6$-tag of cyt c_{553} as means of formation of a stable cyt c_{553} monolayer (see Fig. 2). The cross-sectional SEM analysis showed a well-defined layer of His$_6$-tagged cyt c_{553} captured on the SLG surface trough the conductive pyr-NTA-Ni interface (see Fig. 2 and S3).

We subsequently proceeded to the comprehensive electrochemical characterization of the L1-L3 SLG/pyr-NTA-Ni/cyt nanoassemblies using a cyclic voltammetry (CV) approach which enables to identify the potential values of the redox moieties and provides information about the efficiency of charge transfer. Direct electrochemical analysis of cyt *c* immobilized on the graphene or graphene derivatives electrode surface is challenging as several components of the system can affect the detection of the well-defined redox peaks of this protein mainly due to slow ET kinetics between cyt and graphene [40,41]. In order to properly dissect contribution of cyt to the redox behavior of the biofunctionalized SLG/FTO electrode, the L1 variant of cyt c_{553} was first studied in an aqueous electrolyte solution using FTO/SLG as a WE (Fig. 3A). In the potential window used, the FTO/SLG is redox inactive between −0.2 V and 0.6 V *vs* Ag/AgCl. After the addition of the cyt protein, a couple of redox peaks is identified, with an oxidation peak at 0.12 V and a reduction peak at 0.03 V, confirming ET between SLG and the heme group of cyt *c*. To compare the redox behavior of the different cyt *c* variants immobilized on the SLG surface, SLG/pyr-NTA-Ni and SLG/pyr-NTA-Ni/cyt 19AA constructs were used as the control samples.

The latter control contained the 19AA cyt c_{553} variant described in our previous study [22] which was used for comparison of the electrochemical performance of the novel cyt *c* variant-functionalized electrodes. The 19AA peptide linker forms an L-shaped semi-helical hinged structure predicted to allow for a large conformational flexibility of the immobilized cyt *c* protein in contrast to the 7AA L1-L3 peptide linkers which exhibit a much smaller degree of rotational movement of this protein upon its anchoring onto the electrode surface [15].
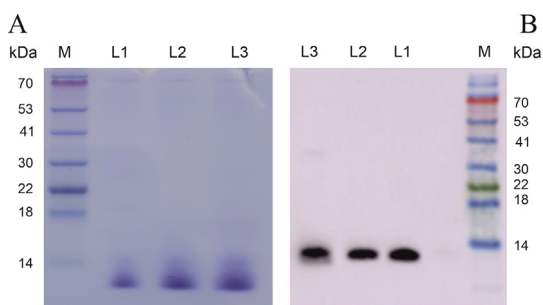
Fig. 1. Biochemical characterization of purified His$_6$-tagged cyt c_{553} variants. A, SDS-PAGE protein profiles of the purified L1-L3 cyt c_{553} variants (1.5 μg protein per lane). B, chemiluminescent detection of the His$_6$-tag within the purified cyt c_{553} L1-L3 variants using a HisProbe. M, protein size marker; L1-L3, fractions of eluted cyt c_{553} variants containing L1-L3 peptide linkers genetically engineered between the *C*-terminal His$_6$-tag and cyt holoprotein.
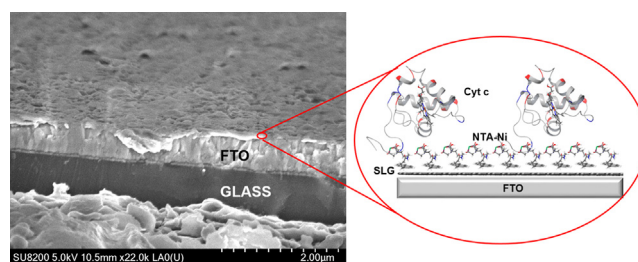
Fig. 2. Cross-sectional SEM imaging of glass/FTO substrate covered with SLG functionalized with the pyr-NTA-Ni/L1 nanoconstruct. The SLG/pyr-NTA-Ni construct forms an ultra-thin layer with a thickness of ∼1.4 nm. The His$_6$-tagged 7AA cyt c_{553} variant (L1 nanoconstruct shown here for the representative SEM imaging) forms a thin layer (thickness of ∼40 nm) upon its capture on pyr-NTA-Ni SAM. Scale bar is 2 μm. *Inset:* Schematic representation of the FTO/SLG/pyr-NTANi/cyt c_{553} nanoconstruct (PDB coordinates for cyt c_6: 1GDV[26]).

A

B
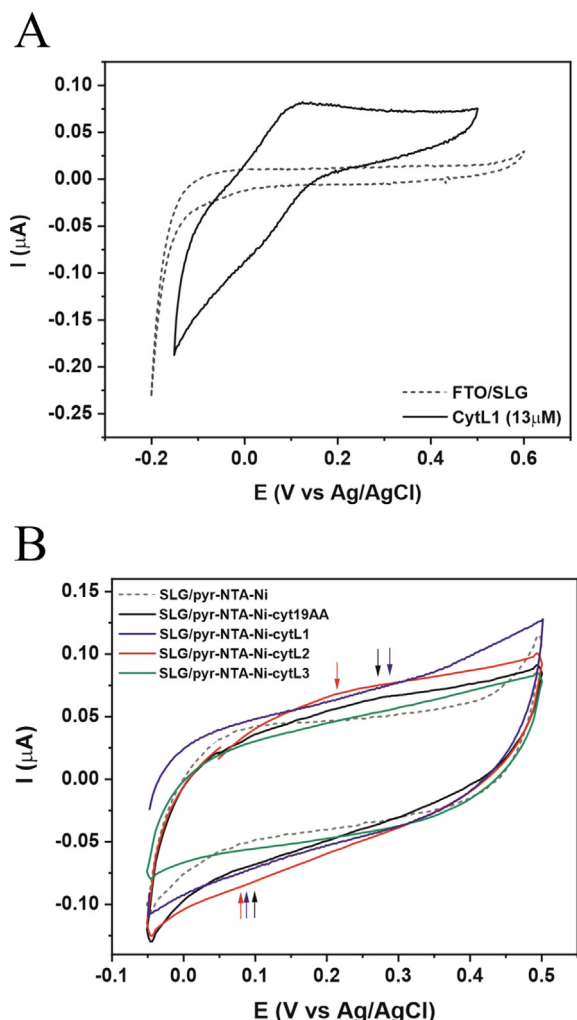
Fig. 3. Cyclic voltammetry of cytochrome c_{553} variants. A, Cyclic voltammetry of FTO/SLG sample before and after the addition of the L1 variant of cyt c_{553} (13 μM) to the electrolyte. B, Cyclic voltammetry analysis of the biohybrid nanoassemblies containing 7AA peptide linker cyt variants on a pyrene-modified graphene monolayer. The electrodes containing the pyr-NTA-Ni SAM without and with 19AA cyt variant were used as control samples. Electrolyte: argon-saturated 5 mM phosphate buffer (pH 7.0). Redox peaks are indicated with arrows for each nanoassembly. Scan rate: 5 mV·s^{-1}.

The CV analysis revealed a pair of small redox peaks between 0.5 V and −0.05 V *vs* Ag/AgCl compared to the redox inactive signature of SLG/pyr-NTA-Ni SAM confirming the presence of the electroactive monolayer of cyt c_{553} on SLG (see Fig. 3B and Fig. S4). Assuming that the concentration of the cyt *c* is similar on all electrodes, the current intensity recorded is mostly governed by the charge transfer efficiency between the redox active heme group, organic interface and the SLG surface (Butler-Volmer equation)[42]. Fig. 3B and Fig. S4 show small redox contribution for the bioassemblies containing the cytochrome 19AA, L1 and L2 variants. In the case of the L3 variant, the CV profile is rather similar to the one of the SLG/pyr-NTA-Ni sample devoid of cyt c_{553}, which implies a reduced capability of DET in the case of the L3 nanoconstruct compared to the other counterparts. The reversible oxidation/reduction peaks were recorded at ~0.27 V and 0.1 V for the 19AA control sample, whereas in the case of the L2-based electrode these potentials were negatively shifted around to ~0.24 V and 0.07 V, respectively (see Fig. 3B). In the case of the L1-based nanoassembly the oxidation/reduction peaks are detected around 0.3 V and 0.08 V respectively, showing a positive shift compared to the 19AA

control. Interestingly, the CV analysis of all cyt-based devices shows a strong positive shift compared to the analysis of the cytochrome in electrolyte solution, which highlights stabilization of the redox process after immobilization of the proteins on the electrode surface.

The occurrence of the enhanced DET occurring within the L1 bioelectrode was independently confirmed by the photochronoamperometric analysis to measure the photocurrent production over a short period of the light ON/ light OFF stimulus (see Fig. 4). The photocurrents in this study are generated mainly through conversion of light absorbed by graphene, and to much smaller extend by FTO since cyt *c* is photochemically inactive. Mechanistically, the origin of the graphene-derived photocurrents has been attributed to either thermoelectric or photovoltaic effects [43]. Graphene has interesting optoelectronic properties due to its zero bandgap, electron–hole symmetry, and high carrier mobility. Introduction of the bio-organic interface to the graphene electrode (such as pyrene-NTA-Ni/cyt SAM of this study) results in opening of the bandgap and enhancing the DET from graphene to the redox active moieties of the interface, both being the critical issues for the successful construction of functional electronic devices.

A

B
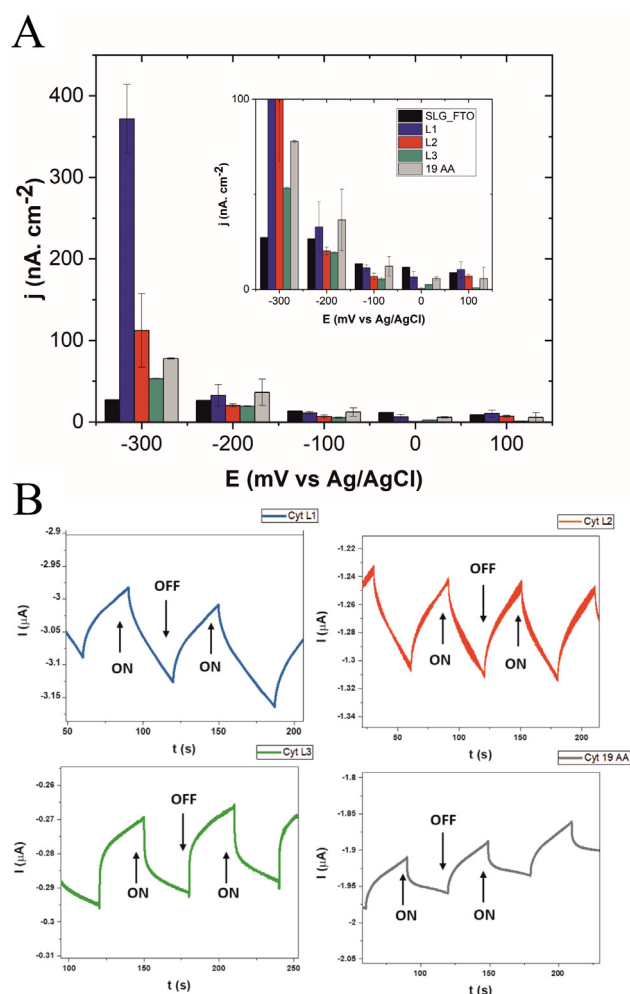
Fig. 4. Photochronoamperometric analysis of the biohybrid cyt c_{553}-based nanoassemblies. A, Photocurrent densities were obtained from the freshly prepared SLG/pyr-NTA-Ni/cyt 19AA (n = 4), cyt 7AA L1 (n = 3), cyt 7AA L2 (n = 2) and cyt 7AA L3 electrodes (n = 2). Inset shows the enlarged fragment of the same chart for better clarity. B, Photocurrents generated from SLG/pyr-NTA-Ni/cyt L1- 19AA variants during chronoamperometric analysis under 30 s. light/dark cycles. Electrolyte: 5 mM phosphate buffer (pH 7.0).

At a −300 mV overpotential, the highest photocurrent was obtained for the L1-containing sample reaching 371.8 nA·cm^{-2}, which corresponds to an over 4.8-fold increase compared to the 19AA cyt control sample. The current density obtained for the L2 sample was 1.4-fold higher than for the 19AA control sample, whereas the photocurrent output was 0.6-fold lower for the L3 nanoconstruct compared to the same control. Thus, we have confirmed that the L1 linker being one of the *in silico* designed 7AA peptides [15] promotes efficient cathodic DET when inserted into the cyt c_{553} structure likely due to exerting the optimal distance and orientation of heme with respect to the SLG surface (see below). The markedly larger photocurrents observed at a −300 mV overpotential compared to the lower bias are likely due to the formation of an energy barrier in the nanoconstructs in the form of the activation overpotential or surface overpotential [44]. The existence of such a barrier between the graphene monolayer and cyt c_{553} biolayer could explain the observed lack of significant differences in the photocurrent output at lower overpotentials.

Overall, the most significant enhancement of the photocurrent output was obtained for the L1 nanoassembly across the whole applied potential range compared to all the other bioelectrodes analyzed in this study (see Fig. 4).

In order to examine the stability and the total photocurrent output of the L1-L3 nanoconstructs, we recorded the photocurrents from each bioelectrode upon continuous standard illumination for up to 1 h under aerobic conditions. The L1 bioelectrode exhibited the highest stability with a mere drop of 1.1%, while the L2 and L3 cyt c variants showed 4.1% and 16.7% decrease of the photocurrent output, respectively (see Fig. S5 and Tab. S1). The maximum photocurrent output of the cyt c_{553}-based nanoassemblies was directly dependent on the variant used as the biotic module of the nanodevice. The current output obtained for the samples after 1 h of continuous illumination (see Fig. S5) was divided by the surface area of the working electrode to obtain current density values. The current density obtained for the L1 sample was 13.9 μA, while the current density values were 4.7 μA, 2.5 μA and 0.7 μA respectively for the L2, L3 and 19 AA control assemblies (see Tab. S1). Overall, the L1 nanoassembly showed a 20-fold higher photocurrent production compared to the 19AA control sample showing its good potential for future applications in bioelectronics. The data obtained from the stability analysis are fully in line with the results of CV and photochronoamperometric analyses.

3.3. Modeling of the direct electron transfer in cytochrome/graphene nanoassemblies

To gain an insight into the DET mechanism occurring between SLG, pyr-NTA-Ni SAM and novel peptide linker cyt c_{553} variants, we performed theoretical simulations, considering a multiscale approach. Initially, we analyzed the conformational space of the three interfaces by means of molecular dynamics (MD) simulations, while in the second step we applied hybrid QM/MM methods to assess the electronic properties of the conductive interface. In MD calculations we observed that all three interfaces are stable in time, and that the three peptide linkers introduced into the *C*-terminal domain of cyt c_{553} do not significantly affect the cyt protein structure, suggesting no or little loss of biological function of this protein upon its immobilization on SLG (details of MD results are reported in Table S2 and Fig. S6 to S9).

The analysis of the geometries of the three interfaces reveals the effect of the peptide linkers on the orientation and position of the heme group, which in turn, reflects the strength of van der Waals interactions between the various amino acid residues of the peptide linkers and SLG. The chemical composition of the peptide linker variants strongly affects the distance between the SLG and

linker (and, accordingly the entire cyt c_{553} protein) as well as the mode of protein interaction with SLG. For the L3 nanoconstruct, we found the minimum SLG-7AA linker distance to be around 0.4 nm, which steadily increases to 0.75 nm and to 1.03 nm for the L1 and L2 counterparts, respectively (Fig. S10). This directly translates into a relatively short heme/SAM distance of 0.90 nm for L3 and L1 samples, which increases to 1.25 nm for L2 (Figs. 5 and 6) and may have direct implication on DET.

It is worth remembering that these are average values, and along the enhancement of DET is the tilting of the heme group with respect to the SLG plane. Figs. 5 and 6 show that three different heme tilting distributions can be observed depending on the linkers. L3 shows an almost perpendicular orientation of 73° to SLG, L2 has a more parallel orientation of 20°, whilst L1 attains an intermediate tilt orientation peaking at 51°. We observed that, although not directly involved in the ET process at the interface, the peptide linkers play a crucial role in determining the position and orientation of the heme group with respect to the SAM/SLG interface (see Fig. S9 and S10).

The three different heme tilting distributions are likely to translate into different degrees of DET efficiency, a feature that was confirmed by the electrochemical analysis. To obtain a quantitative description of the DET processes we considered a hybrid QM/MM approach. From the 50 extracted heme/NTA pair structures, the distribution of the frontier molecular orbitals (FMO) and their localization over the different fragments were analyzed.

As noted above, the three interfaces differ not only in the tilt of the heme group, but also in the distance and orientation over the NTA molecule. From the QM/MM calculations on extracted pairs of heme/NTA molecules, we computed the minimum distance between them. L2 shows a flat orientation of heme with respect to SLG and a distance of 0.95 nm, while for L3 the distance is only 0.57 nm, but the carboxylic groups point away from the NTA moiety (see Fig. S11 for representative snapshots). A summary of the QM/MM results is reported in Table 2. DD Despite the presence of only one distribution of relative orientations for the L1 interface (Fig. S12), two different FMO distributions are found. The major localized excitation (LE) on the NTA molecule, representing the 80% of the transitions, is from the pyrene to the Ni metal center, but there is also a second excitation (20% of the transitions) responsible for the charge transfer (CT) from the pyrene to the heme group (Fig. 7). Both distributions represent a net DET flow moving away from the pyrene moiety and towards the metal centers, thus rationalizing the observed enhanced cathodic current for the L1 variant electrode over and above the L2 and L3 counterparts (see Fig. 4). For both transitions the HOMO distribution is strongly
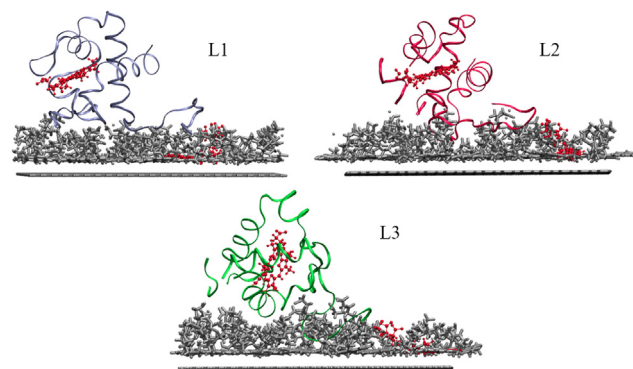
Fig. 5. Schematic representations of the studied L1-L3 interfaces after 200 ns MD simulations. The cyt protein is depicted in blue (L1), dark red (L2) and green (L3) while the NTA molecule coordinated to His$_6$-tag is depicted in red. The remaining NTA molecules and SLG are depicted in grey. Water molecules are not shown for clarity.
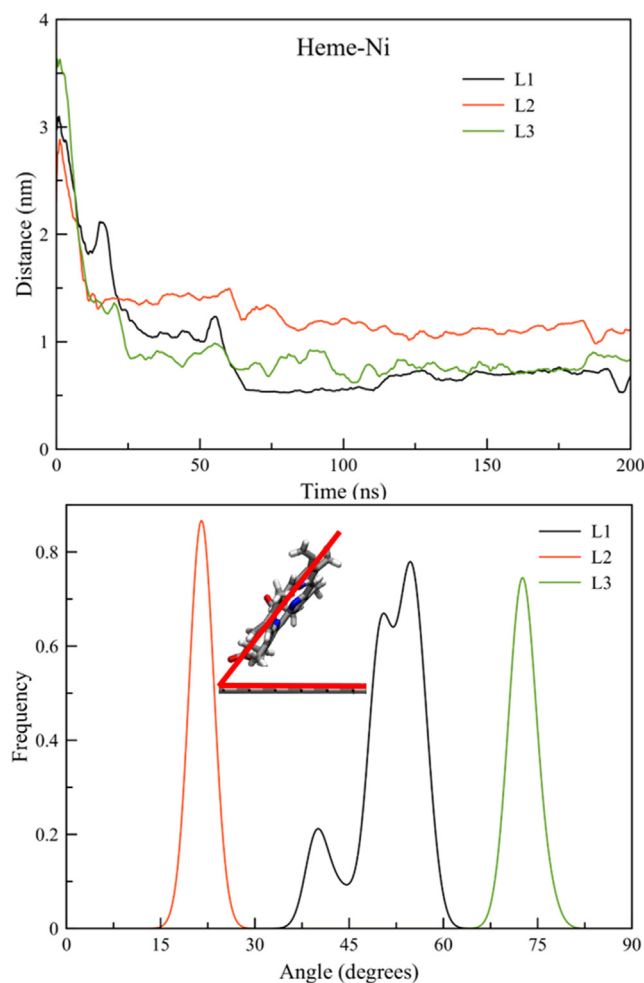
Fig. 6. Minimum distance analysis between the heme and Ni moieties of the interfaces (top) and heme tilt angle distribution (bottom) with respect to the SLG layer. The inset shows the tilt angle between electrode flat surface and the heme group.

localized over a narrow energy range with a maximum peak at −5.94 eV and −5.75 eV for LE and CT, respectively. For the LUMO, a bigger spread of the energies is found, with maximum values at −3.53 eV and −3.93 eV (see Table 2). These results translate into an average energy gap opening of 2.46 eV and 1.90 eV for LE and CT, respectively.

Different HOMO values and FMO localization were found for the other two interfaces corresponding to the L2 and L3 peptide linker variants of cyt c_{553}. For both systems, the HOMO levels are strongly localized over the heme porphyrin fragment while the LUMOs are localized over the NTA-Ni cation moiety, leading to a strong CT of electrons from the heme to the NTA. For these interfaces, both HOMO and LUMO distributions are narrow, with maximum peaks at −5.23 (−7.08) and −2.81 (−5.42) eV, leading to an average energy gap of 2.41 (1.62) eV for L2 (L3). The difference between

the L2 and L3 interfaces resides in the orientation and distance of the heme group from the NTA molecule. In fact, while for the L2 cyt variant the heme group is oriented parallel to the pyrene moiety, for the L3 variant it is almost perfectly perpendicular. In addition, the distances between the NTA moiety and the heme group strongly differ, decreasing from a relatively large value of 0.95 nm for L2 to 0.57 nm for L3.

Thus, an anodic current is expected to be enhanced for the electrodes modified with the L2 and L3 peptide linker variants of cyt. Our combined electrochemical analysis and theoretical modelling provide a holistic picture behind the mechanism of DET occurring between SLG, pyr-NTA-Ni SAM and the cyt holoprotein, whereby the relatively short peptide linkers of varying AA composition affect strongly the DET features derived in turn from the differential orientation and distance of the heme group with respect to the SLG/SAM surface. We propose that a perpendicular or parallel orientation of the heme group is detrimental for the cathodic current generation and DET, as observed for L2 and L3 samples, in which the electrons flow from the heme to the NTA moiety of SAM. On the other hand, a tilt angle of 50° predicted for the L1 variant electrode is the value for which a strong DET from NTA to heme occurs. This tilt angle identified for the anchored L1 cyt variant results in two different charge distributions, a major one localized over the NTA molecule (LE component of DET corresponding to CT from pyr to NTA-Ni moiety) and a minor one localized over the two redox components of the bio-organic interface (CT component of DET corresponding to CT from pyr to heme moieties), with both bearing the HOMO localized over the pyrene group. Such cyt conformation on the SLG surface results in electrons flowing toward the heme group, thus allowing for the observed enhanced cathodic photocurrent generation.

The DFT calculations presented in this work can be directly compared only to the experimental measurements when a bias is not applied. Then, the behavior of charge transfer can be extrapolated when an overpotential is applied. When an anodic potential is applied (positive bias, 100 mV), we observe an enhancement of current in the L2 sample, while for the L3 device almost no current is generated due to strong charge recombination and the presence of the insulating alpha helix of the protein between the heme and the SAM-forming molecule. In the case of the cathodic overpotential (−100, −200 and −300 mV) when the external bias is high enough, it overcomes the internal flux of charges, thus determining the direction of the DET. The DET modeling results are therefore in a good agreement with the electrochemical data.

A semi-quantitative assessment of the DET mechanism involved (tunneling *vs*. hopping) is considered here, in analogy to previous studies on this topic. [45] From this model, three main parameters are needed, namely the driving force (which is obtained from CV measurements), the distance between the donors and acceptors and their energy gap, which are obtained from computation (for the full discussion on the method see the Supplementary Information). From this analysis we can define a threshold energy Ec which determines the nature of the DET with respect to the energy gap (Eg) computed; if Ec > Eg, a hopping mechanism is favored, while the opposite is true when Ec < Eg. By applying this approach, it was observed that for all the studied interfaces Eg > Ec, thus the

Table 2
Average distance of the heme/NTA pairs (in nm) and frontier molecular orbitals energetic analysis (in eV) for the three investigated interfaces from QM/MM simulation.

Heme/NTA pairs	Distance	HOMO	LUMO	Energy Gap
L1 (LE)	0.50	−5.94 (±0.29)	−3.53 (±0.54)	2.46 (±0.51)
L1 (CT)	0.50	−5.75 (±0.18)	−3.93 (±0.48)	1.90 (±0.53)
L2	0.95	−5.23 (±0.32)	−2.81 (±0.66)	2.41 (±0.82)
L3	0.57	−7.08 (±0.32)	−5.42 (±0.38)	1.62 (±0.44)

Distances are reported in nm, energies in eV. The reported values are averaged over the 50 extracted snapshots. The standard deviation is shown in brackets.
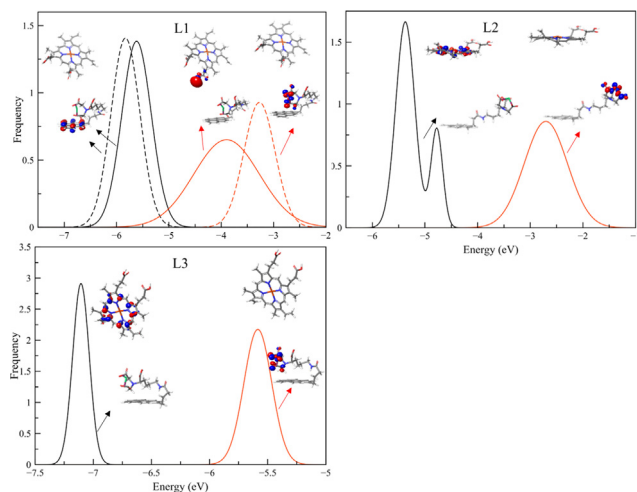
Fig. 7. FMOs distribution for the three interfaces studied. Insets show the shapes of the HOMO and LUMO orbitals.

tunneling mechanism prevails, although for the L1-based nanoassembly, SLG is the donor and cyt is the acceptor, whereas for the L2 and L3-based samples the opposite direction of electron flow occurs (see details in Supplementary Information). To rationalize this electronic behavior, we have to consider that at the relatively short distances between the heme group and SLG predicted for all the nanodevices in this study, reorientation and immobilization of the cyt protein in the most favorable configuration for DET becomes rate determining.

Due to the asymmetry of the heme group inside the cyt structure, different orientations of this moiety define its different distances from the electrode surface, which in turn determines the kinetics of DET and the resultant photocurrent output. In particular, the L3 sample represents the most thermodynamic stable nanoconstruct, with the shortest distance between heme and SLG. However, the observed DET is not as high as for the L1 sample. Moreover, no protein domains are predicted by MD simulations to be present between the heme and NTA moiety for the L1 sample, while large domains of the protein are likely to be inserted in the same region of the interface for both the L2 and L3 counterparts. This strongly suggests that the heme orientation promoting the highest DET does not have to overlap with those exhibiting the highest interaction energies. At short distances (like the ones discussed in the present work), the orientation of the protein is the key factor to consider for the efficiency of DET and even small conformational fluctuations exert a fine tuning of DET. Moreover, the different orientation of the protein backbone, determined by the dipole moment of the heme group (with carboxylic groups pointing toward/away from the SAM) defines the final orientation of cytochrome over the assembly, in turn determining the DET kinetics. According to our calculations, maximum DET is obtained by direct contact between the heme edge and the SAM surface, as observed for the L1 structure, indicating that the DET kinetics is controlled by an interplay between protein conformational dynamics and ET tunneling probabilities. This conclusion agrees with the reported studies of cyt c physisorbed on the alkylthiol SAM/Au electrode [46]. It is worth noting, however, that the DET properties may be strongly affected by different factors such as angular orientation of the heme, its distance to the SAM and the presence of the protein backbone in between the two redox systems, which ultimately is determined by the peptide linker sequence. The combination of all these factors determine the electron flow which has been shown theoretically and experimentally to occur even when the peptide linkers are not present [15,38,47].

Importantly, even small structural changes within the linker may strongly affect the DET properties, which can be dissected in depth only by a combined approach of the QM/MM modelling and electrochemical investigation.

4. Conclusions

The combined electrochemical data in conjunction with the quantum mechanical analysis demonstrate that the AA sequence of the relatively short novel peptide linkers, genetically engineered between the anchoring His_6-tag and the holoprotein of cyt c_{553}, plays a crucial role for the efficient electronic interaction between the heme group of this model redox-active protein, the conductive organic interface (pyr-NTA) and the graphene monolayer. This finding is in line with the possibility of chemically control the charge transfer using the tryptophan in a peptide chain [48]. The AA sequence of the linkers affects the electronic response not only in terms of the amount of photocurrent generated, but also the directionality of the electron flow. This work confirms the possibility of fine-tuning the electronic properties of complex bio-organic interfaces by means of introducing the rationally designed peptide linkers within the cyt c_{553} structure, which in turn, can lead to the desired electronic response due to the optimized tilt angle of the heme group, its distance from the electrode surface as well as the optimal HOMO/LUMO levels of the interacting redox moieties within the bio-organic interface. In agreement with the previous works, we report here that the orientation and distance between the heme group of cytochrome c and the electrode can affect significantly the overall photocurrent output [15,17]. Furthermore, this study paves the way for the rational design of efficient bio-nanoassemblies (in terms of enhanced DET and preferred directionality of electron flow) by genetic engineering of the short, rationally designed peptide linkers within the molecular structure of electroactive proteins, which can yield the significantly improved performance of various types of nanodevices including biosensors, biohybrid solar cells and solar-to-fuel devices. Indeed, one of the novel devices described in this study (L1 variant-based bioelectrode) yielded a ~20-fold enhancement of the photocurrent output compared to the previously described nanodevices of a similar type, confirming the applicability of this simple, yet rational approach for improvement of the bioelectronic device efficiency and stability.

5. Authorship statement

MI: investigation, validation, visualization, writing the original draft; SO: formal analysis, writing the original draft; MJ, MK: investigation, validation, review and editing; AS, BT: formal analysis; EH, CGU, KO: investigation, resources; AŁ, TU, PN, DB: assistance in molecular cloning; JK: conceptualization, methodology, writing the original draft, review and editing, project administration and funding acquisition.

Declaration of Competing Interest

The authors declare that they have no known competing financial interests or personal relationships that could have appeared to influence the work reported in this paper.

Acknowledgements

Technologies, University of Warsaw (internal grant no. 501-D313-86-0119600-01 to MI and SO).

Appendix A. Supplementary material

Supplementary data to this article can be found online at https://doi.org/10.1016/j.bioelechem.2021.107818.

References

[1] J. Kargul, M. Kiliszek, Artificial photosynthesis, in: Bioelectrochemical Interface Engineering, John Wiley & Sons, Ltd, 2019: pp. 271–309. https://doi.org/10.1002/9781119611103.ch15.

[2] N. Kornienko, J.Z. Zhang, K.K. Sakimoto, P. Yang, E. Reisner, Interfacing nature's catalytic machinery with synthetic materials for semi-artificial photosynthesis, Nat. Nanotechnol. 13 (2018) 890–899, https://doi.org/10.1038/s41565-018-0251-7.

[3] S. Osella, J. Kargul, M. Izzo, B. Trzaskowski, Architecture and Function of Biohybrid Solar Cell and Solar-to-Fuel Nanodevices, in: E.V. Levchenko, Y.J. Dappe, G. Ori (Eds.), Theory and Simulation in Physics for Materials Applications: Cutting-Edge Techniques in Theoretical and Computational Materials Science, Springer International Publishing, Cham, 2020, pp. 227–274, https://doi.org/10.1007/978-3-030-37790-8_13.

[4] S.K. Ravi, V.S. Udayagiri, L. Suresh, S.C. Tan, Emerging role of the band-structure approach in biohybrid photovoltaics: A path beyond bioelectrochemistry, Adv. Funct. Mater. 28 (2018) 1705305, https://doi.org/10.1002/adfm.201705305.

[5] A. Ruff, F. Conzuelo, W. Schuhmann, Bioelectrocatalysis as the basis for the design of enzyme-based biofuel cells and semi-artificial biophotoelectrodes, Nat Catal. 3 (2020) 214–224, https://doi.org/10.1038/s41929-019-0381-9.

[6] C.D. Bostick, S. Mukhopadhyay, M. Sheves, D. Cahen, D. Lederman, Protein bioelectronics: a review of what we do and do not know, (n.d.) 158.

[7] V.P. Hitaishi, R. Clement, N. Bourassin, M. Baaden, A. De Poulpiquet, S. Sacquin-Mora, A. Ciaccafava, E. Lojou, Controlling redox enzyme orientation at planar electrodes, Catalysts 8 (2018) 192, https://doi.org/10.3390/catal8050192.

[8] S. Osella, M. Kiliszek, E. Harputlu, C.G. Unlu, K. Ocakoglu, J. Kargul, B. Trzaskowski, Controlling the charge transfer flow at the graphene/pyrene–nitrilotriacetic acid interface, J. Mater. Chem. C. 6 (2018) 5046–5054, https://doi.org/10.1039/C8TC00564H.

[9] X. Gao, K. Ni, C. Zhao, Y. Ren, D. Wei, Enhancement of the activity of enzyme immobilized on polydopamine-coated iron oxide nanoparticles by rational orientation of formate dehydrogenase, J. Biotechnol. 188 (2014) 36–41, https://doi.org/10.1016/j.jbiotec.2014.07.443.

[10] S. Ma, C.V.F.P. Laurent, M. Meneghello, J. Tuoriniemi, C. Oostenbrink, L. Gorton, P.N. Bartlett, R. Ludwig, Direct electron-transfer anisotropy of a site-specifically immobilized cellobiose dehydrogenase, ACS Catal. 9 (2019) 7607–7615, https://doi.org/10.1021/acscatal.9b02014.

[11] M. Campàs, B. Prieto-Simón, J.-L. Marty, A review of the use of genetically engineered enzymes in electrochemical biosensors, Semin. Cell Dev. Biol. 20 (2009) 3–9, https://doi.org/10.1016/j.semcdb.2009.01.009.

[12] F. Lopez, T. Siepenkoetter, X. Xiao, E. Magner, W. Schuhmann, U. Salaj-Kosla, Potential pulse-assisted immobilization of Myrothecium verrucaria bilirubin oxidase at planar and nanoporous gold electrodes, J. Electroanal. Chem. 812 (2018) 194–198, https://doi.org/10.1016/j.jelechem.2017.12.023.

[13] N.D.J. Yates, M.A. Fascione, A. Parkin, Methodologies for "Wiring" redox proteins/enzymes to electrode surfaces, Chemistry. 24 (2018) 12164–12182, https://doi.org/10.1002/chem.201800750.

[14] Á. Szűcs, M. Novák, Stable and reversible electrochemistry of cytochrome c on bare electrodes Part II: Effects of experimental conditions, J. Electroanal. Chem. 384 (1995) 47–55, https://doi.org/10.1016/0022-0728(94)03741-K.

[15] J.D. Janna Olmos, P. Becquet, D. Gront, J. Sar, A. Dąbrowski, G. Gawlik, M. Teodorczyk, D. Pawlak, J. Kargul, Biofunctionalisation of p-doped silicon with cytochrome c553 minimises charge recombination and enhances photovoltaic performance of the all-solid-state photosystem I-based biophotoelectrode, RSC Adv. 7 (2017) 47854–47866, https://doi.org/10.1039/C7RA10895H.

[16] C.A. Bortolotti, M. Borsari, M. Sola, R. Chertkova, D. Dolgikh, A. Kotlyar, P. Facci, Orientation-dependent kinetics of heterogeneous electron transfer for Cytochrome c immobilized on gold: electrochemical determination and theoretical prediction, J. Phys. Chem. C. 111 (2007) 12100–12105, https://doi.org/10.1021/jp072813g.

[17] N. Amdursky, D. Ferber, C.A. Bortolotti, D.A. Dolgikh, R.V. Chertkova, I. Pecht, M. Sheves, D. Cahen, Solid-state electron transport via cytochrome c depends on electronic coupling to electrodes and across the protein, PNAS 111 (2014) 5556–5561, https://doi.org/10.1073/pnas.1319351111.

[18] Y. Dai, D.A. Proshlyakov, G.M. Swain, Effects of film morphology and surface chemistry on the direct electrochemistry of Cytochrome c at boron-doped diamond electrodes, Electrochim. Acta 197 (2016) 129–138, https://doi.org/10.1016/j.electacta.2016.02.032.

[19] K.R. Stieger, S.C. Feifel, H. Lokstein, F. Lisdat, Advanced unidirectional photocurrent generation via cytochrome c as reaction partner for directed assembly of photosystem I, Phys. Chem. Chem. Phys. 16 (2014) 15667–15674, https://doi.org/10.1039/C4CP00935E.

[20] H. Ju, S. Liu, B. Ge, F. Lisdat, F.W. Scheller, Electrochemistry of Cytochrome c immobilized on colloidal gold modified carbon paste electrodes and its electrocatalytic activity, Electroanalysis 14 (2002) 141–147, https://doi.org/10.1002/1521-4109(200201)14:2<141::AID-ELAN141>3.0.CO;2-Y.

[21] M. Szalkowski, E. Harputlu, M. Kiliszek, C.G. Unlu, S. Maćkowski, K. Ocakoglu, J. Kargul, D. Kowalska, Plasmonic enhancement of photocurrent generation in a photosystem I-based hybrid electrode, J. Mater. Chem. C. (2020), https://doi.org/10.1039/C9TC06983F.

[22] M. Kiliszek, E. Harputlu, M. Szalkowski, D. Kowalska, C.G. Unlu, P. Haniewicz, M. Abram, K. Wiwatowski, J. Niedziółka-Jönsson, S. Maćkowski, K. Ocakoglu, J. Kargul, Orientation of photosystem I on graphene through cytochrome c553 leads to improvement in photocurrent generation, J. Mater. Chem. A. 6 (2018) 18615–18626, https://doi.org/10.1039/C8TA02420K.

[23] C.J. Faulkner, S. Lees, P.N. Ciesielski, D.E. Cliffel, G.K. Jennings, Rapid assembly of photosystem I monolayers on gold electrodes, Langmuir 24 (2008) 8409–8412, https://doi.org/10.1021/la800670b.

[24] B. Wang, Enhanced biological hydrogen production from Escherichia coli with surface precipitated cadmium sulfide nanoparticles, Adv. Energy Mater. 7 (2017).

[25] J.D. Janna Olmos, J. Kargul, A quest for the artificial leaf, Int. J. Biochem. Cell Biol. 66 (2015) 37–44, https://doi.org/10.1016/j.biocel.2015.07.005.

[26] Z. Chen, S. Berciaud, C. Nuckolls, T.F. Heinz, L.E. Brus, Energy transfer from individual semiconductor nanocrystals to graphene, ACS Nano 4 (2010) 2964–2968, https://doi.org/10.1021/nn1005107.

[27] Y. Wang, D. Kurunthu, G.W. Scott, C.J. Bardeen, Fluorescence quenching in conjugated polymers blended with reduced graphitic oxide, J. Phys. Chem. C. 114 (2010) 4153–4159, https://doi.org/10.1021/jp9097793.

[28] M. Twardowska, D. Chomicki, I. Kamińska, J. Niedziółka-Jönsson, S. Maćkowski, Fluorescence imaging of hybrid nanostructures composed of natural photosynthetic complexes and reduced graphene oxide, Nanospectroscopy. (2015). https://www.degruyter.com/view/journals/nansp/open-issue/article-10.1515-nansp-2015-0002/article-10.1515-nansp-2015-0002.xml.

[29] L. Banszerus, M. Schmitz, S. Engels, J. Dauber, M. Oellers, F. Haupt, K. Watanabe, T. Taniguchi, B. Beschoten, C. Stampfer, Ultrahigh-mobility graphene devices from chemical vapor deposition on reusable copper, Sci Adv. 1 (2015), https://doi.org/10.1126/sciadv.1500222 e1500222.

[30] S. Chaudhury, S. Lyskov, J.J. Gray, PyRosetta: a script-based interface for implementing molecular modeling algorithms using Rosetta, Bioinformatics 26 (2010) 689–691, https://doi.org/10.1093/bioinformatics/btq007.

[31] D.W. Russell, J. Sambrook, Molecular cloning: a laboratory manual, Cold Spring Harbor Laboratory Cold Spring Harbor, NY, 2001.

[32] M. Matsuzaki, O. Misumi, T. Shin-i, S. Maruyama, M. Takahara, S. Miyagishima, T. Mori, K. Nishida, F. Yagisawa, K. Nishida, Y. Yoshida, Y. Nishimura, S. Nakao, T. Kobayashi, Y. Momoyama, T. Higashiyama, A. Minoda, M. Sano, H. Nomoto, K. Oishi, H. Hayashi, F. Ohta, S. Nishizaka, S. Haga, S. Miura, T. Morishita, Y. Kabeya, K. Terasawa, Y. Suzuki, Y. Ishii, S. Asakawa, H. Takano, N. Ohta, H. Kuroiwa, K. Tanaka, N. Shimizu, S. Sugano, N. Sato, H. Nozaki, N. Ogasawara, Y. Kohara, T. Kuroiwa, Genome sequence of the ultrasmall unicellular red alga Cyanidioschyzon merolae 10D, Nature 428 (2004) 653–657, https://doi.org/10.1038/nature02398.

[33] M.J. Abraham, T. Murtola, R. Schulz, S. Páll, J.C. Smith, B. Hess, E. Lindahl, GROMACS: High performance molecular simulations through multi-level parallelism from laptops to supercomputers, SoftwareX. 1–2 (2015) 19–25, https://doi.org/10.1016/j.softx.2015.06.001.

[34] A.D. Mackerell Jr., Empirical force fields for biological macromolecules: Overview and issues, J. Comput. Chem. 25 (2004) 1584–1604, https://doi.org/10.1002/jcc.20082.

[35] T. Yanai, D.P. Tew, N.C. Handy, A new hybrid exchange-correlation functional using the Coulomb-attenuating method (CAM-B3LYP), Chem. Phys. Lett. 393 (2004) 51–57, https://doi.org/10.1016/j.cplett.2004.06.011.

[36] P.J. Hay, W.R. Wadt, Ab initio effective core potentials for molecular calculations. Potentials for the transition metal atoms Sc to Hg, J. Chem. Phys. 82 (1985) 270–283, https://doi.org/10.1063/1.448799.

[37] A.D. Bochevarov, E. Harder, T.F. Hughes, J.R. Greenwood, D.A. Braden, D.M. Philipp, D. Rinaldo, M.D. Halls, J. Zhang, R.A. Friesner, Jaguar: A high-performance quantum chemistry software program with strengths in life and materials sciences, Int. J. Quantum Chem. 113 (2013) 2110–2142, https://doi.org/10.1002/qua.24481.

[38] A.M. Kowalska, B. Trzaskowski, S. Osella, Assessing the charge transfer at the Cytochrome c553/graphene interface: a multiscale investigation, J. Phys. Chem. C. 122 (2018) 29405–29413, https://doi.org/10.1021/acs.jpcc.8b10517.

[39] H. Akazaki, F. Kawai, H. Chida, Y. Matsumoto, M. Hirayama, K. Hoshikawa, S. Unzai, W. Hakamata, T. Nishio, S.-Y. Park, T. Oku, Cloning, expression and purification of cytochrome c6 from the brown alga Hizikia fusiformis and complete X-ray diffraction analysis of the structure, Acta Crystallograph. Section F. 64 (2008) 674–680.

[40] Z.S. Aghamiri, M. Mohsennia, H.-A. Rafiee-Pour, Immobilization of cytochrome c and its application as electrochemical biosensors, Talanta 176 (2018) 195–207, https://doi.org/10.1016/j.talanta.2017.08.039.

[41] S. Gupta, A. Irihamye, Probing the nature of electron transfer in metalloproteins on graphene-family materials as nanobiocatalytic scaffold using electrochemistry, AIP Adv. 5 (2015), https://doi.org/10.1063/1.4914186 037106.

[42] E.J.F. Dickinson, A.J. Wain, The Butler-Volmer equation in electrochemical theory: Origins, value, and practical application, J. Electroanal. Chem. 872 (2020), https://doi.org/10.1016/j.jelechem.2020.114145 114145.

[43] M. Freitag, T. Low, F. Xia, P. Avouris, Photoconductivity of biased graphene, Nat. Photonics 7 (2013) 53–59, https://doi.org/10.1038/nphoton.2012.314.

[44] W. Wang, X. Wei, D. Choi, X. Lu, G. Yang, C. Sun, Chapter 1 - Electrochemical cells for medium- and large-scale energy storage: fundamentals, in: C. Menictas, M. Skyllas-Kazacos, T.M. Lim (Eds.), Advances in Batteries for Medium and Large-Scale Energy Storage, Woodhead Publishing, 2015, pp. 3–28, https://doi.org/10.1016/B978-1-78242-013-2.00001-7.

[45] A.A. Voityuk, Long-range electron transfer in biomolecules. Tunneling or hopping?, J. Phys. Chem. B. 115 (2011) 12202–12207, https://doi.org/10.1021/jp2054876.

[46] D. Alvarez-Paggi, D.F. Martín, P.M. DeBiase, P. Hildebrandt, M.A. Martí, D.H. Murgida, Molecular basis of coupled protein and electron transfer dynamics of Cytochrome c in biomimetic complexes, J. Am. Chem. Soc. 132 (2010) 5769–5778, https://doi.org/10.1021/ja910707r.

[47] S. Alwarappan, R.K. Joshi, M.K. Ram, A. Kumar, Electron transfer mechanism of cytochrome c at graphene electrode, Appl. Phys. Lett. 96 (2010), https://doi.org/10.1063/1.3458698 263702.

[48] C. Guo, X. Yu, S. Refaely-Abramson, L. Sepunaru, T. Bendikov, I. Pecht, L. Kronik, A. Vilan, M. Sheves, D. Cahen, Tuning electronic transport via hepta-alanine peptides junction by tryptophan doping, PNAS 113 (2016) 10785–10790, https://doi.org/10.1073/pnas.1606779113.